This PDF file includes:

Figures S1 to S8
Tables S1
Uncropped original images of Western blot

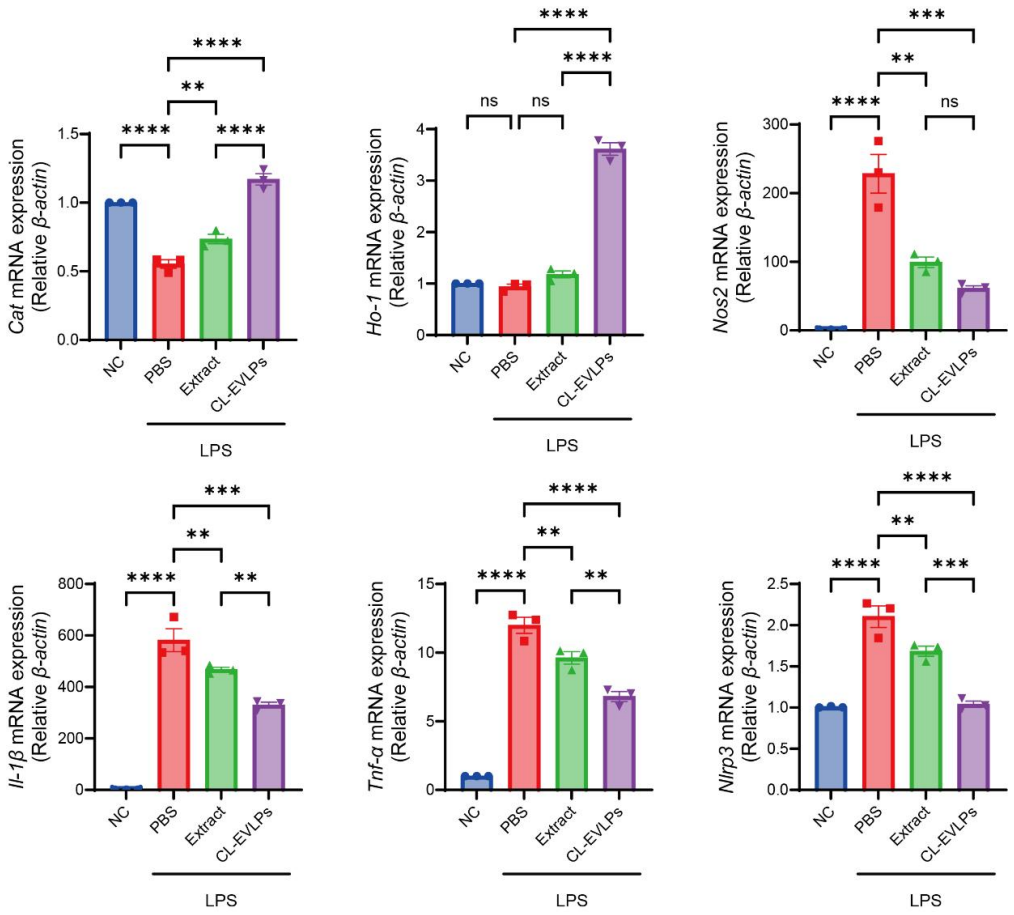

Figure S1. Comparison of anti-inflammatory and antioxidant effects of CL-EVLPs and crude turmeric extract in LPS-stimulated BV2 cells. n = 3; one-way ANOVA, ns: not statistically significant; **p < 0.01, ***p < 0.001, ****p < 0.0001.

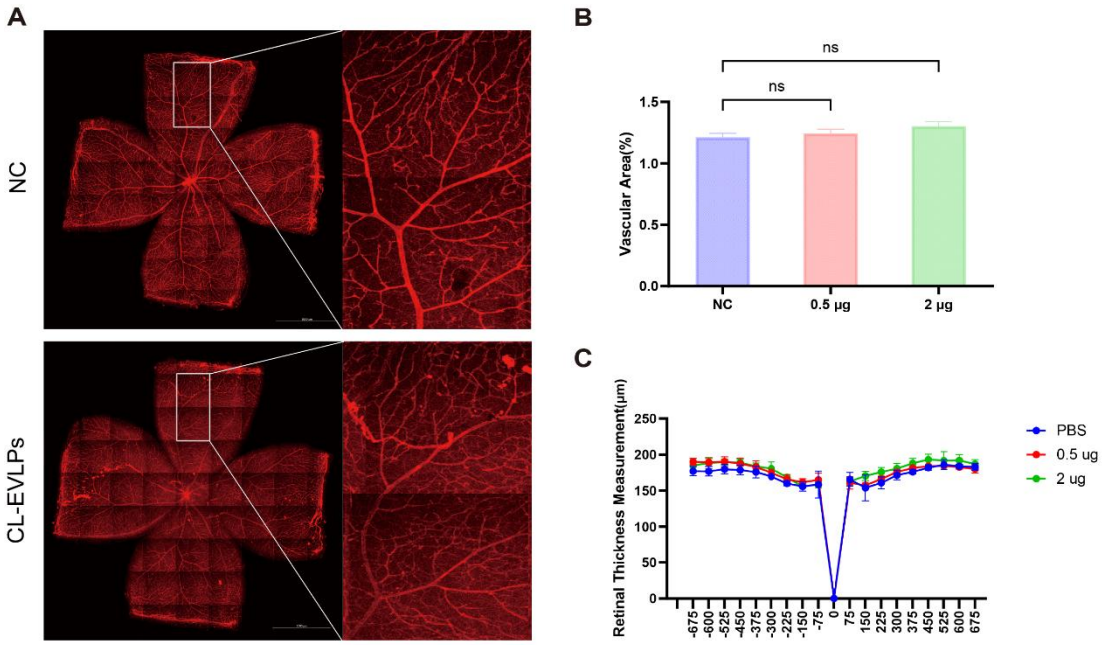

Figure S2. Biological safety evaluation of intravitreally injected CL-EVLPs (A) Immunofluorescence staining of retinal vasculature in eyes injected with CL-EVLPs versus the control group. (B) Quantification of vascular area. n = 3, ns: not statistically significant. (C) Quantification of retinal thickness by OCT. n = 3. No significant differences were observed among the three groups (two- way ANOVA).

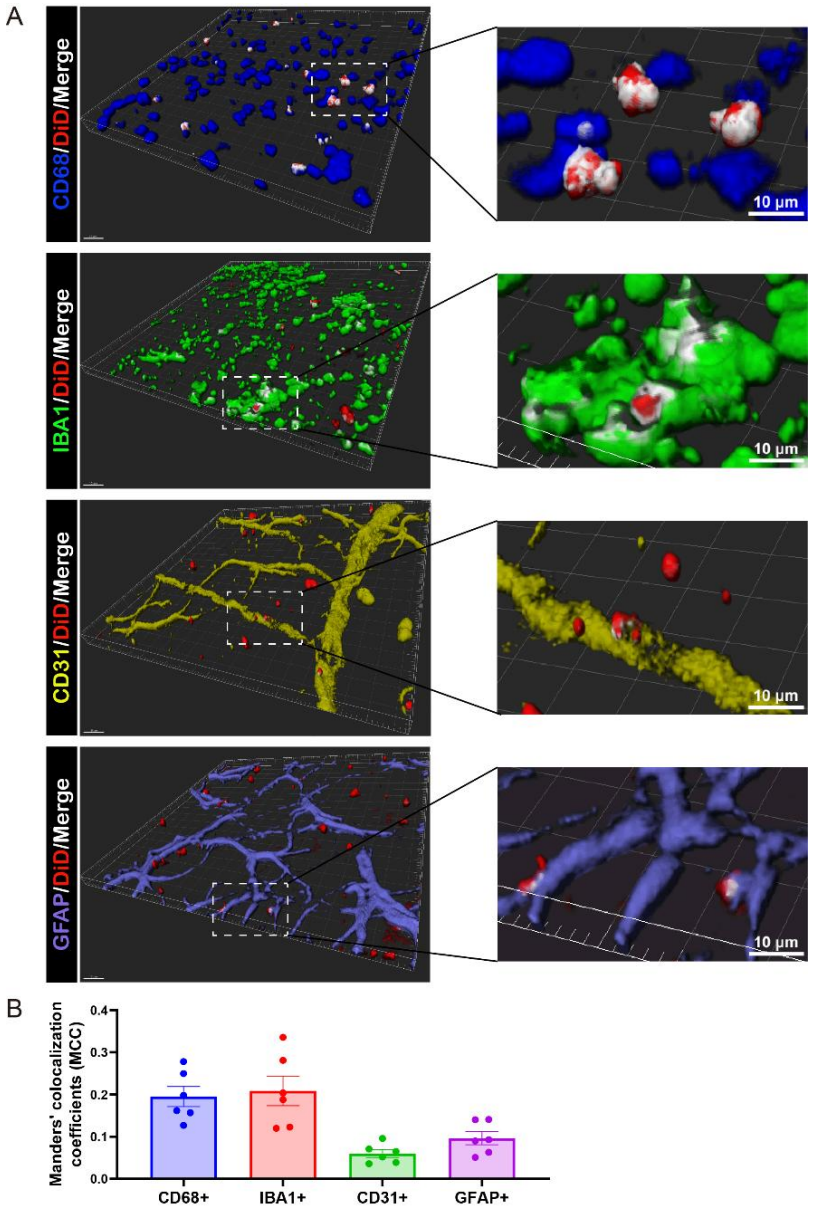

Figure S3. 3D reconstruction of DiD – CL-EVLPs distribution and cell-type colocalization in the retina. (A) Representative 3D surface-rendered images showing colocalization between DiD-labeled CL-EVLPs (red) and $CD68^{+}$ macrophages (blue), $IBA1^{+}$ microglia (green), $CD31^{+}$ endothelial cells (yellow), and $GFAP^{+}$ astrocytes (purple). Boxed regions are shown at higher magnification on the right. Scale bar, 10 μm. (B) Quantification of colocalization between DiD–CL-EVLPs and each cell type using Manders' colocalization coefficient (MCC). Data are presented as mean ± SEM.

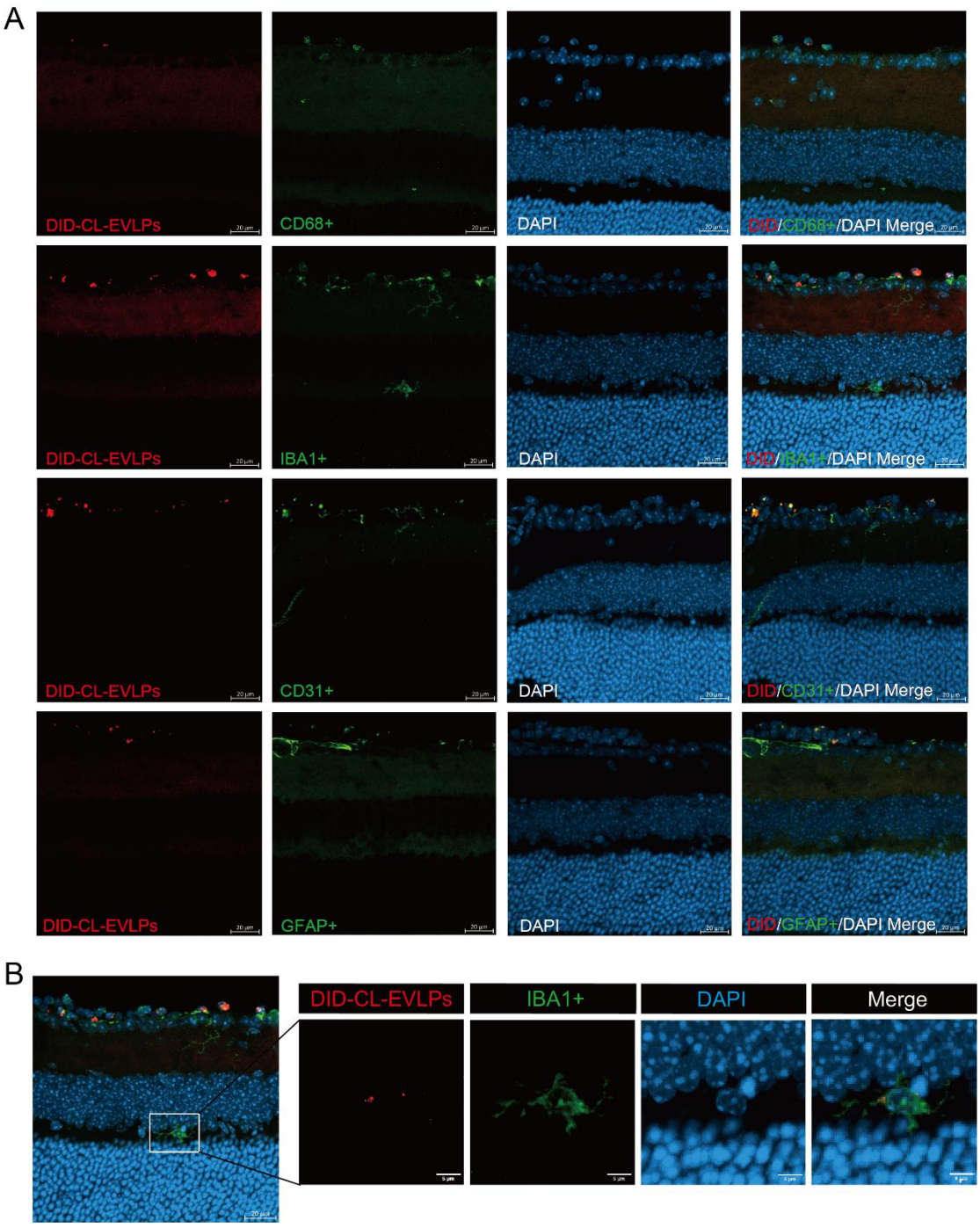

Figure S4. Colocalization analysis of DiD−CL-EVLPs with different retinal cell types in retinal sections. (A) Representative immunofluorescence images of retinal cross-sections showing colocalization of DiD-labeled CL-EVLPs (red) with $CD68^{+}$ macrophages, $IBA1^{+}$ microglia, $CD31^{+}$ endothelial cells, and $GFAP^{+}$ astrocytes. Nuclei were counterstained with DAPI (blue), and merged images are presented on the right. (B) Higher-magnification view of the boxed region, demonstrating the colocalization signal between DiD–CL-EVLPs and $IBA1^{+}$ microglia. Scale bars are indicated in the images.

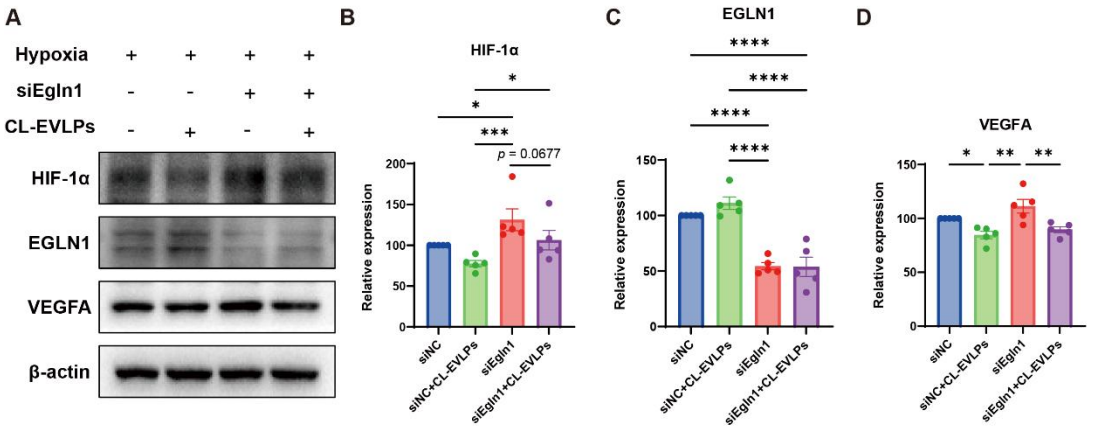

Figure S5. Effect of CL-EVLPs on the HIF-1α/VEGFA signaling axis following Egln1 knockdown in hypoxia-stimulated BV2 cells. (A) Immunoblot analysis of HIF-1α, EGLN1, and VEGFA in hypoxia-treated BV2 cells following transfection with siEgln1 and treatment with CL-EVLPs. (B–D) Quantification of HIF-1α, EGLN1, and VEGFA protein levels; one-way ANOVA; *p < 0.05, **p < 0.01, ***p < 0.001, ****p < 0.0001.

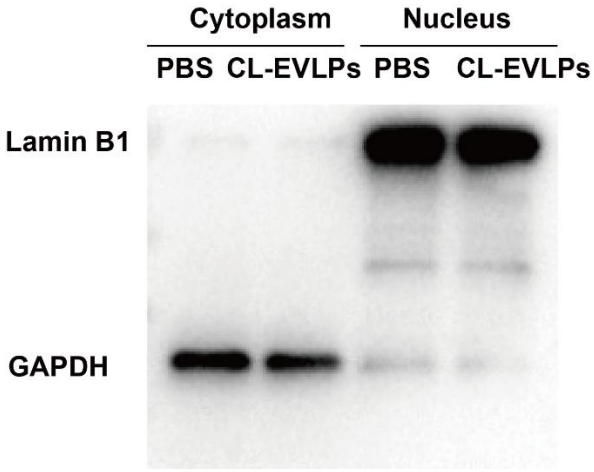

Figure S6. Validation of nuclear and cytoplasmic fraction purity in OIR mouse retinas. Representative immunoblots of cytoplasmic and nuclear extracts from OIR mouse retinas treated with PBS or CL-EVLPs. Lamin B1 and GAPDH were employed as nuclear and cytoplasmic markers, respectively, to verify efficient subcellular fractionation.

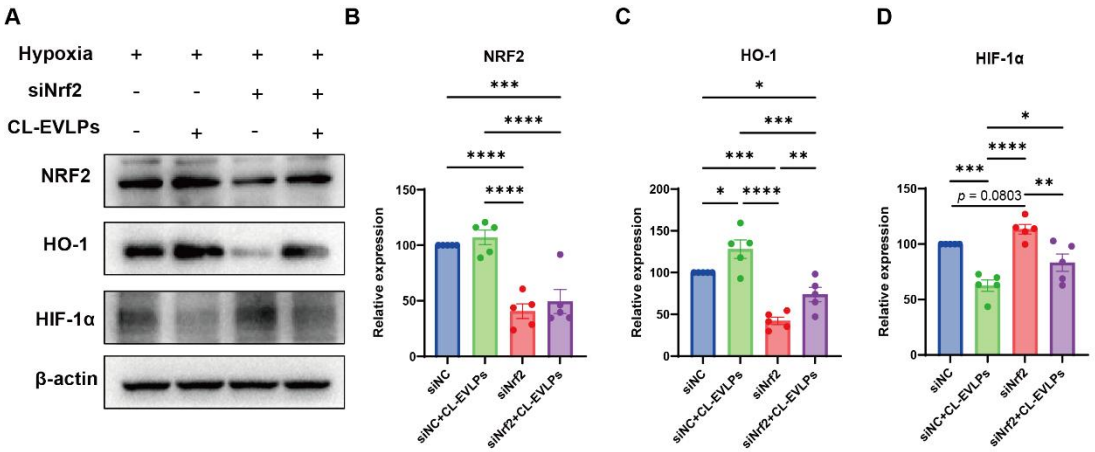

Figure S7. Effect of CL-EVLPs on the NRF2/HO-1 signaling axis following *Nrf2* knockdown in hypoxia-stimulated BV2 cells. (A) Immunoblot analysis of NRF2, HO-1, and HIF-1α protein levels. (B–D) Quantification of NRF2, HO-1, and HIF-1α protein expression; one-way ANOVA; *p < 0.05, **p < 0.01, ***p < 0.001, ****p < 0.0001.

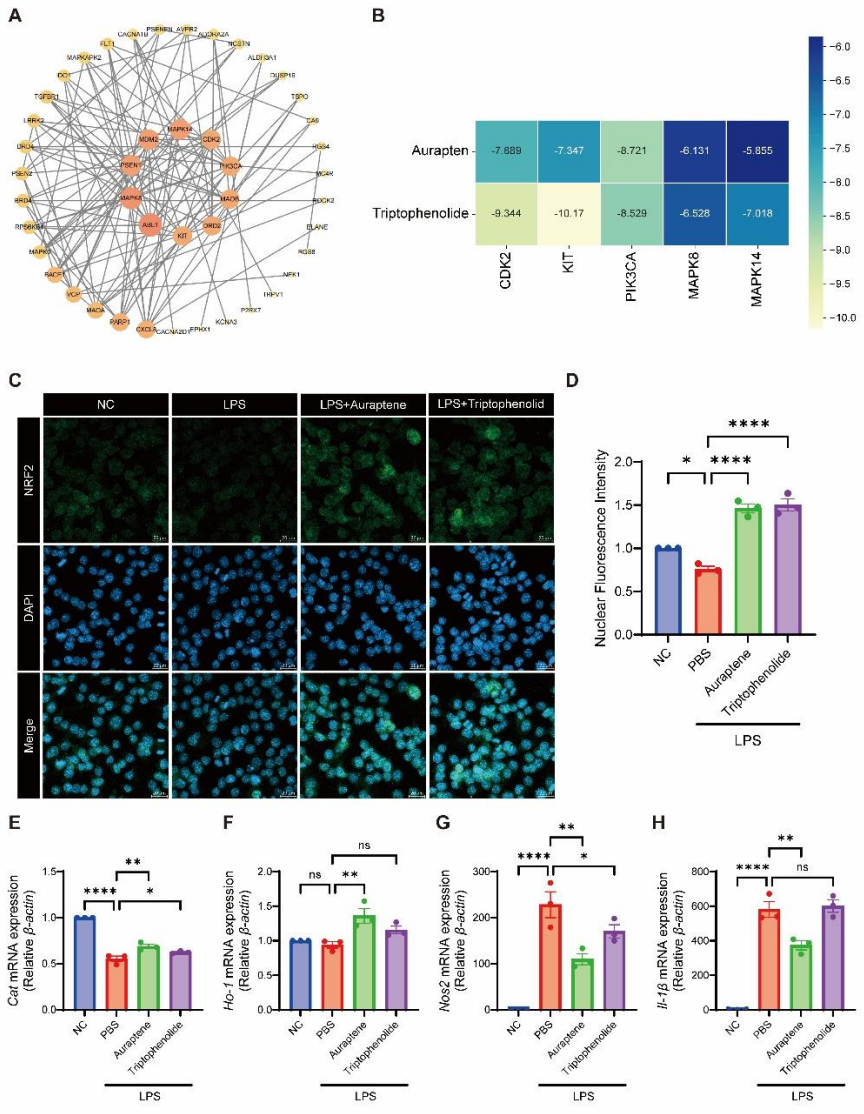

Figure S8. Auraptene and triptophenolide: hub-target docking and modulation of inflammation and oxidative stress. (A) Protein–protein interaction network. (B) Heatmap of binding affinities for auraptene and triptophenolide docked to CDK2, KIT, PIK3CA, MAPK8, and MAPK14. (C – D) Immunofluorescence images showing enhanced NRF2 nuclear translocation following auraptene and triptophenolide treatment in LPS-stimulated BV2 cells. (E–H) Auraptene and triptophenolide suppress LPS-induced mRNA expression of *Nos2* and *Il-1β*, while elevating *Ho-1* and *Cat* in BV2 cells; n = 3; one-way ANOVA; ns, not significant; *p < 0.05, **p < 0.01, ****p < 0.0001.

Tables S1

Table S1. List of siRNAs.

Target *	siRNA Name	Antisense Sequence (5′→3′)
Egln1 (mmu)	si-Egln1-1	UACAUGUCACGCAUCUUCCAU
	si-Egln1-2	UUGUGCUUCUUCCAGUCCUGG
	si-Egln1-3	UUCAAUGUCAGCAAACUGGGC
Nrf2 (mmu)	si-Nrf2-1	UACUCCAAGAUCUAUGUCUUG
	si-Nrf2-2	UUCUCCUGUUUCUUCAUCCAG
	si-Nrf2-3	CACAAAAGACAAACAUUCAAG
Negative control (mmu)	si-NC	UUCUCCGAACGUGUCACGU

Uncropped original images of Western blot

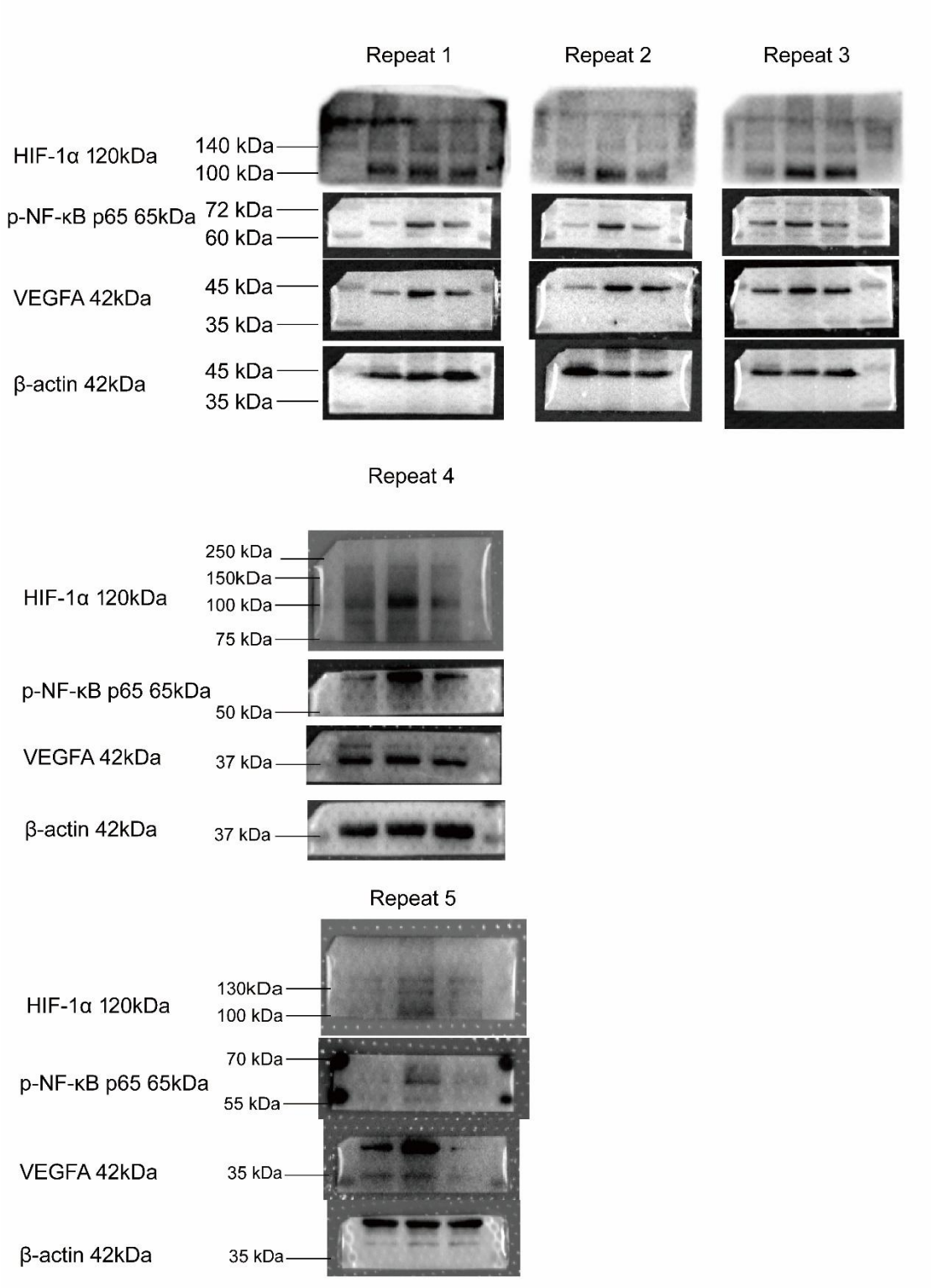

Full, uncropped Western blot membranes corresponding to the cropped blots presented in Figure 5 of the main manuscript. This figure shows the original membranes for HIF-1α, p-NF-κB p65, VEGFA, and β-actin. Exposure time, antibody information, and image acquisition parameters were kept consistent across all experimental

groups.

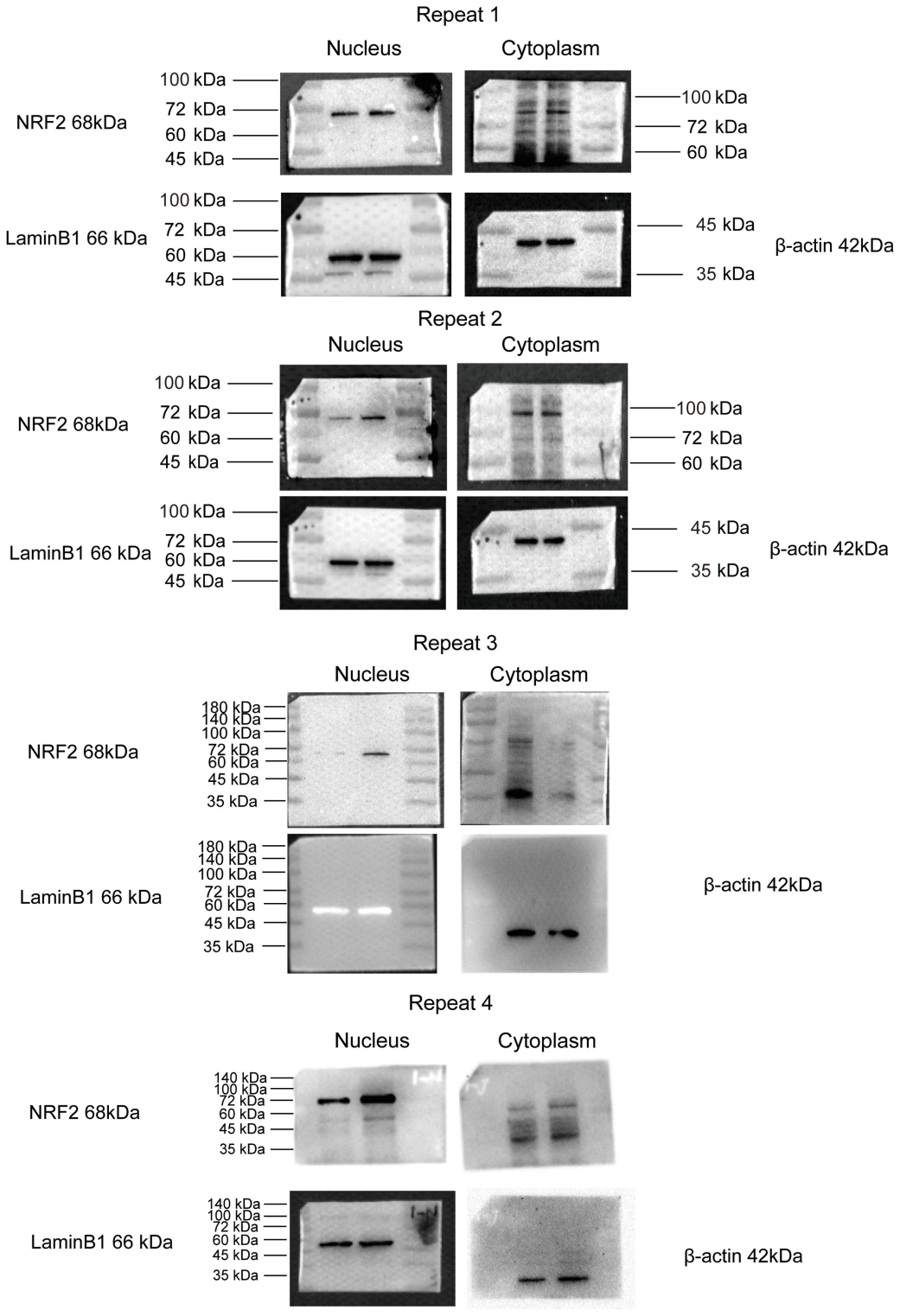

Full, uncropped Western blot membranes corresponding to the cropped blots presented in Figure 6 of the main manuscript. This figure shows the original membranes for NRF2, Lamin B1, and β-actin. Exposure time, antibody information, and image acquisition parameters were kept consistent across experimental groups.

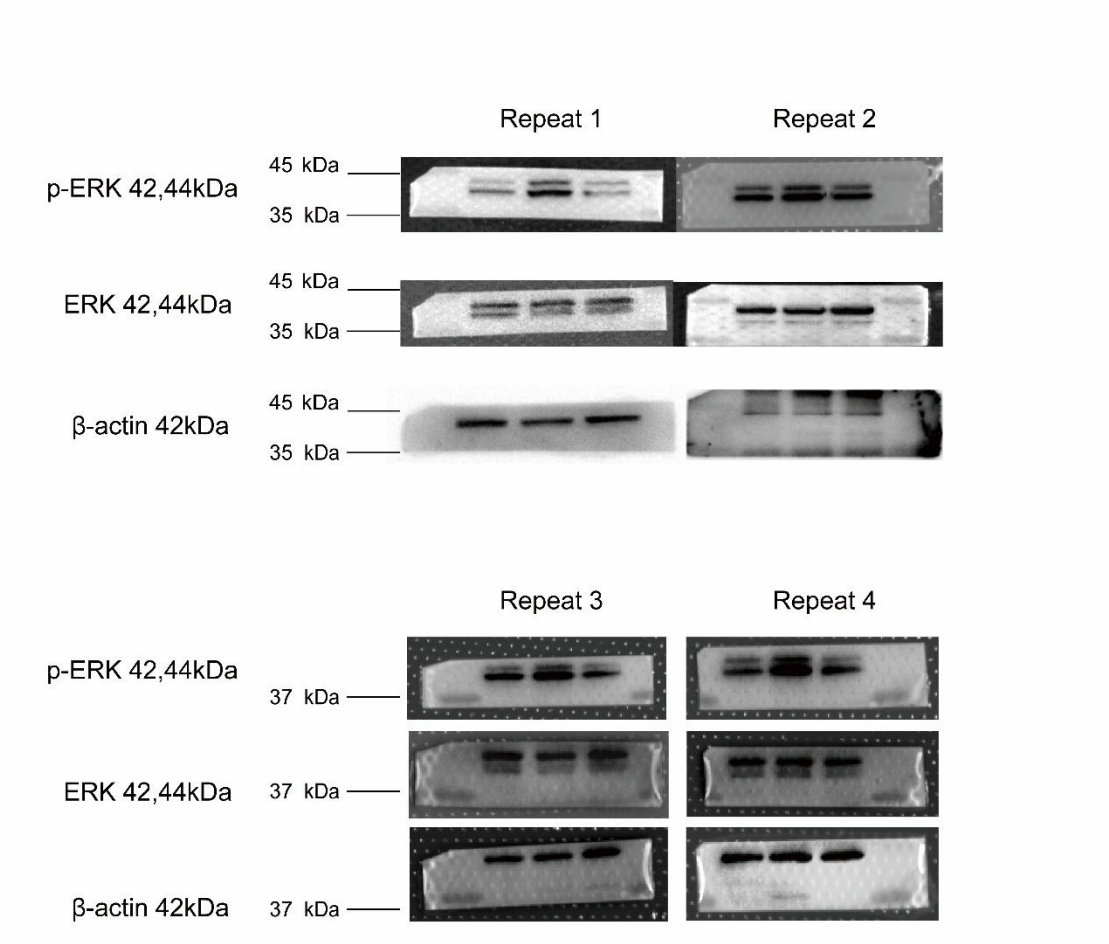

Full, uncropped Western blot membranes corresponding to the cropped blots presented in Figure 7 of the main manuscript. This figure shows the original membranes for P-ERK, ERK, and β-actin. Exposure time, antibody information, and image acquisition parameters were kept consistent across experimental groups.

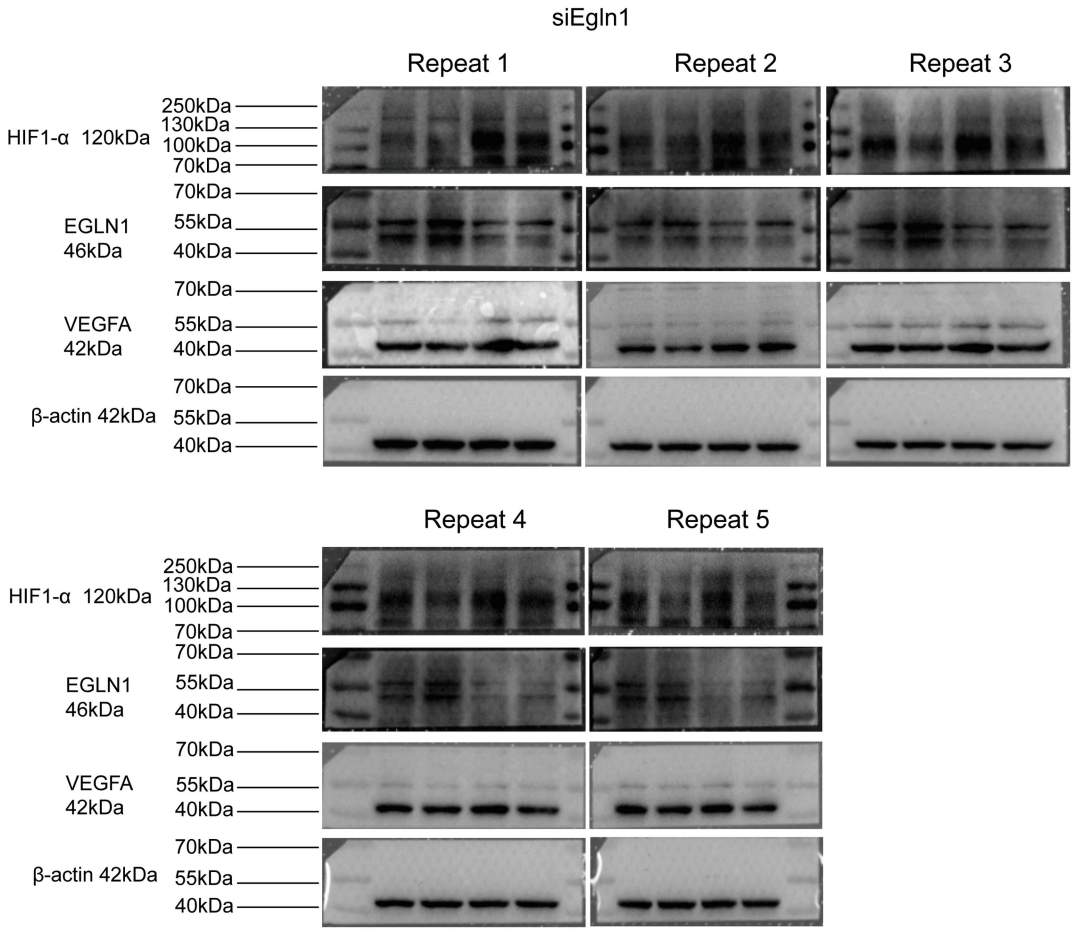

Full, uncropped Western blot membranes corresponding to the cropped blots presented in Figure S5 of the main manuscript. This figure shows the original membranes for HIF-1α, EGLN1, VEGFA and β-actin. Exposure time, antibody information, and image acquisition parameters were kept consistent across experimental groups.

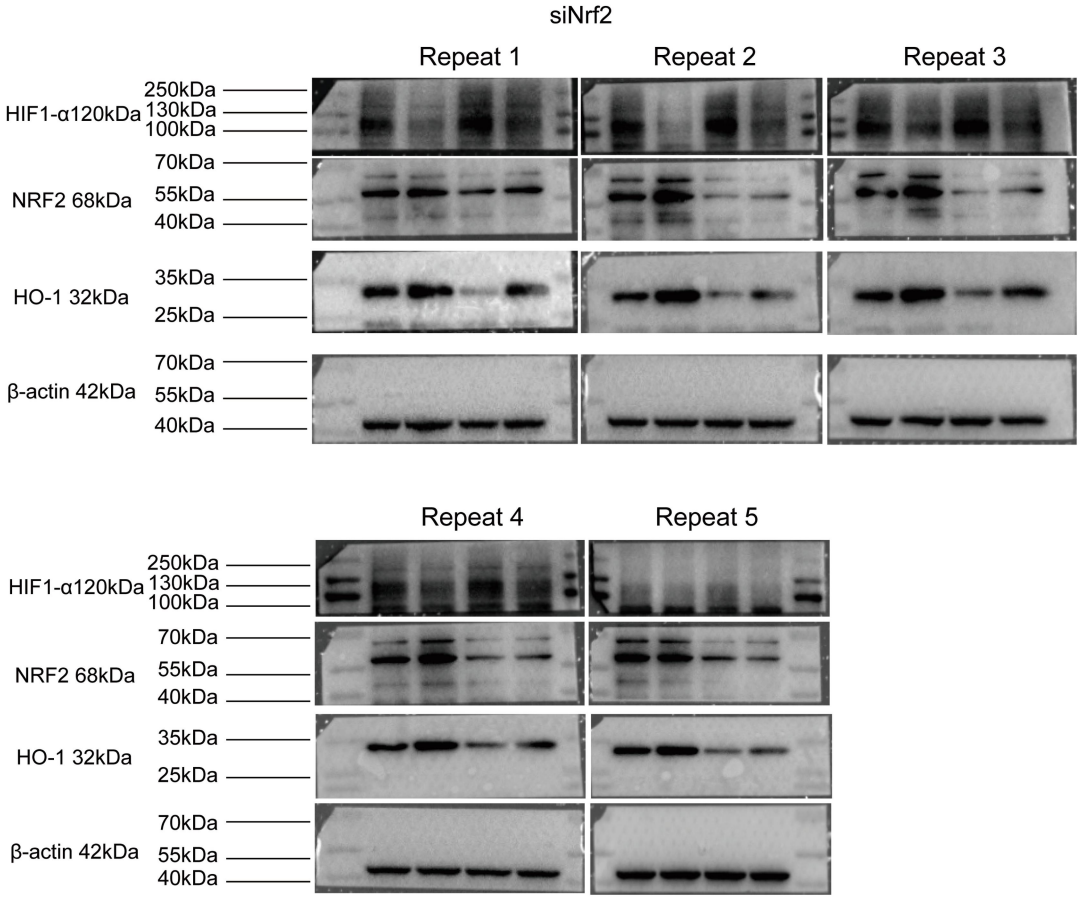

Full, uncropped Western blot membranes corresponding to the cropped blots presented in Figure S7 of the main manuscript. This figure shows the original membranes for HIF-1α, NRF2, HO-1, and β-actin. Exposure time, antibody information, and image acquisition parameters were kept consistent across experimental groups.